Contents lists available at ScienceDirect

Applied Catalysis B: Environmental

BiVO$_4$/3DOM TiO$_2$ nanocomposites: Effect of BiVO$_4$ as highly efficient visible light sensitizer for highly improved visible light photocatalytic activity in the degradation of dye pollutants

Meryam Zalfani [a,b,c], Zhi-Yi Hu [d,**], Wen-Bei Yu [a], Mounira Mahdouani [c], Ramzi Bourguiga [c], Min Wu [a,**], Yu Li [a,**], Gustaaf Van Tendeloo [d], Yahia Djaoued [e], Bao-Lian Su [a,b,f,*]

[a] State Key Laboratory of Advanced Technology for Materials Synthesis and Processing, Wuhan University of Technology, Luoshi Road 122, 430070, Wuhan, Hubei, China
[b] Laboratory of Inorganic Materials Chemistry (CMI), University of Namur, 61 rue de Bruxelles, B-5000 Namur, Belgium
[c] Laboratoire de Physique des Matériaux, Structure et Propriétés, Groupe Physique des Composants et Dispositifs Nanométriques, Faculté des Sciences de Bizerte, University of Carthage, 7021 Jarzouna-Bizerte, Tunisie
[d] EMAT (Electron Microscopy for Materials Science), University of Antwerp, Groenenborgerlaan 171, B-2020 Antwerp, Belgium
[e] Université de Moncton, Campus de Shippagan, 218, boulevard J.-D. Gauthier, Moncton, Canada
[f] Clare Hall, University of Cambridge, Cambridge, United Kingdom

ARTICLE INFO

ABSTRACT

A series of BiVO$_4$/3DOM TiO$_2$ nanocomposites have been synthesized and their photocatalytic activity was investigated under visible light irradiation using the RhB dye as model pollutant molecule in an aqueous solution. The effect of the amount of BiVO$_4$ as visible light sensitizer on the photocatalytic activity of BiVO$_4$/3DOM TiO$_2$ nanocomposites was highlighted. The heterostructured composite system leads to much higher photocatalytic efficiencies than bare 3DOM TiO$_2$ and BiVO$_4$ nanoparticles. As the proportion of BiVO$_4$ in BiVO$_4$/3DOM TiO$_2$ nanocomposites increases from 0.04 to 0.6, the photocatalytic performance of the BiVO$_4$/3DOM TiO$_2$ nanocomposites increases and then decreases after reaching a maximum at 0.2. This improvement in photocatalytic perfomance is related to 1) the interfacial electron transfer efficiency between the coupled materials, 2) the 3DOM TiO$_2$ inverse opal structure with interconnected pores providing an easy mass transfer of the reactant molecules and high accessibility to the active sites and large surface area and 3) the effect of light sensitizer of BiVO$_4$. Intensive studies on structural, textural, optical and surface properties reveal that the electronic interactions between BiVO$_4$ and TiO$_2$ lead to an improved charge separation of the coupled BiVO$_4$/TiO$_2$ system. The photogenerated charge carrier densities increase with increasing the BiVO$_4$ content, which acts as visible light sensitizer to the TiO$_2$ and is responsible for the enhancement in the rate of photocatalytic degradation. However, the photocatalytic activity is reduced when the BiVO$_4$ amount is much higher than that of 3DOM TiO$_2$. Two reasons could account for this behavior. First, with increasing BiVO$_4$ content, the photogenerated electron/hole pairs are accumulated at the surface of the BiVO$_4$ nanoparticles and the recombination rate increases as shown by the PL results. Second, decreasing the amount of 3DOM TiO$_2$ in the nanocomposite decreases the surface area as shown by the BET results. Moreover, the poor adsorptive properties of the BiVO$_4$ photocatalyst also affect the photocatalytic performance, in particular at higher BiVO$_4$ content. The present work demonstrates that BiVO$_4$/3DOM TiO$_2$ is a very promising heterojunction system for visible light photocatalytic applications.

1. Introduction

* Corresponding author at: Laboratory of Inorganic Materials Chemistry (CMI), University of Namur, 61 rue de Bruxelles, Namur, B-5000, Belgium.
** Corresponding authors.
E-mail addresses: zhiyi.hu@uantwerpen.be (Z.-Y. Hu), minwu@whut.edu.cn (M. Wu), yu.li@whut.edu.cn (Y. Li), baoliansu@whut.edu.cn, bao-lian.su@unamur.be, bls26@cam.ac.uk (B.-L. Su).

Semiconductor-based photocatalysis has attracted much attention as a potential solution for dealing with the global energy crisis and environmental pollution [1–4]. Among various types of semiconductors, TiO$_2$ has been the most suitable for widespread environmental applications due to its strong oxidizing ability. How-

ever, its photocatalytic activity under visible light irradiation needs to be enhanced [5–8]. Recently, considerable attention has been paid to the bismuth-based semiconductors [9–13]. Many Bi-based compounds possess a narrow band gap and exhibit high visible-light photocatalytic activity because of their hybridized O 2p and Bi 6s2 valence bands [14,15]. Tremendous efforts have been devoted to the formation of a heterojunction between TiO$_2$ and narrow band gap semiconductors to enhance visible light responding photocatalyst with high activity. Monoclinic BiVO$_4$, having a band gap of ~2.4 eV, has been reported to possess excellent activity under visible irradiation [16–21]. Nevertheless, the rapid recombination rate of electron-hole pairs, the poor charge transport properties and the poor adsorptive behavior are still the main drawback of m-BiVO$_4$. The combination of TiO$_2$ and a sensitizer, BiVO$_4$, leading to the formation of an n heterojunction, can offer promising advantages in the photocatalytic system by improving visible absorption of TiO$_2$ and reducing the recombination rate of electron-hole of BiVO$_4$. With light irradiation, electrons and holes move in opposite direction under the driving of a built in electric-field. The charge carriers are thus separated and the carrier lifetime is prolonged [22,23]. This charge separation prevents the electrons and holes from recombination. Thus, the electrons and holes have more opportunities to participate in reduction and oxidation reactions for the degradation of the organic dye on their surface. The formation of an interface between two semiconductors is an effective strategy in enhancing the separation of photogenerated electrons and holes and thus reducing the recombination rate. The well-matched energy band alignement is a key factor for the achievement of efficient heterojunctions [24,25]. Recently the BiVO$_4$/TiO$_2$ heterojunction has been attracted considerable attention as a promising photocatalyst under visible light irradiation and has shown a significant suppression of the photogenerated electron-hole recombination [26–36]. Li et al. [34] showed that the photocatalytic performance of BiVO$_4$/TiO$_2$ heterojunction is drastically improved by controlling the contact facet owing to an especially high electron transfer capacity between TiO$_2$ and the {110} facet of BiVO$_4$. A suitable energy band alignment was found between both coupled semiconductors. An heterostructured m-BiVO$_4$/{001}-TiO$_2$ with shuriken-like shape was successfully synthesized by Zhu et al. [35] using a facile hydrothermal method. The obtained BiVO$_4$/TiO$_2$ heterojunction possessed a much higher photocatalytic activity for the degradation of methylene blue (MB) under visible light irradiation than the pure BiVO$_4$ and physically mixed BiVO$_4$-TiO$_2$ sample. This was attributed to a higher separation efficiency of the photogenerated electron-hole pairs under visible light irradiation. Xie et al. [32] fabricated BiVO$_4$/TiO$_2$ nanocomposites with different molar ratios and effective contacts by putting BiVO$_4$ nanoparticles into a TiO$_2$ sol, followed by a thermal treatment at 450 °C. The photogenerated charge carriers in the BiVO$_4$/TiO$_2$ nanocomposite with a proper molar ratio of 5% displays a much longer lifetime and a higher separation efficiency than those in BiVO$_4$ alone. This can be attributed to the unusual spatial transfer of visible-excited high-energy electrons of BiVO$_4$ to TiO$_2$. Hu et al. [29] prepared BiVO$_4$/TiO$_2$ with a mass ratio of 1: 200 by a hydrothermal treatment for the benzene degradation reaction and claimed that their material was 3–4 times more active than nitrogen doped TiO$_2$ under visible light irradiation.

Zhang et al. [28] reported the synthesis of BiVO$_4$/TiO$_2$ by a one-step microwave hydrothermal method and found that the 20 wt% TiO$_2$/BiVO$_4$ nanocomposite exhibited better photocatalytic activity than pure monoclinic BiVO$_4$ and other percentages of TiO$_2$ in BiVO$_4$. This is because of its high crystallinity, narrow bandgap, and most importantly, the hierarchical heterostructure which can effectively separate photoinduced electron–hole pairs on the surface of BiVO$_4$/TiO$_2$ photocatalysts. BiVO$_4$/3DOM TiO$_2$ nanocomposites were synthesized for the first time via a hydrothermal method [36]. The results showed that 3DOM BiVO$_4$/TiO$_2$ nanocomposites possess a highly prolonged lifetime and an increased separation efficiency of visible light generated charges and an extraordinarily high photocatalytic activity. Owing to the intimate contact between BiVO$_4$ and large surface area 3DOM TiO$_2$, the photogenerated high energy charges can be easily transferred from BiVO$_4$ to the 3DOM TiO$_2$ support under the internal field induced by the different electronic band structures of the coupled semiconductors. It was also found that the larger the amount of BiVO$_4$ in the nanocomposite, the longer the duration of photogenerated charge separation and the higher the photocatalytic activity. 3DOM structures with an open interconnected porous network can also facilitate the diffusion of molecules and offer a larger surface area which is essential for the accessibility of the dye molecules to the photocatalysts and for a better dispersion of the BiVO$_4$ nanoparticles [37–41]. Therefore BiVO$_4$/3DOM TiO$_2$ nanocomposites show an enhanced photocatalytic efficiency compared with pure 3DOM TiO$_2$, dumbbell-like BiVO$_4$ nanoparticles, physically mixed BiVO$_4$ nanoparticles and 3DOM TiO$_2$ and BiVO$_4$/TiO$_2$ nanocomposites without a 3DOM structure. Although the combination of BiVO$_4$ nanoparticles and 3DOM TiO$_2$ is quite beneficial for photocatalytic activity, it is found that the amount of BiVO$_4$ affects significantly the recombination of photogenerated electron-holes, the visible light sensitizing efficiency, electron transfer from the BiVO$_4$ to TiO$_2$ and thus finally the photocatalytic activity. It is crucial to know how the amount of BiVO$_4$ will influence the formation of the heterojunction between BiVO$_4$ nanoparticles and 3DOM TiO$_2$. Since the photocatalytic reactions occur at the side of TiO$_2$ (conduction and valence band of TiO$_2$), it is important to know how a decreasing TiO$_2$ amount and an increasing BiVO$_4$ amount will modify the photocatalytic efficiency of BiVO$_4$/3DOM TiO$_2$ nanocomposites to design photocatalyts with best performance. Photocatalytic efficiency of the BiVO$_4$/3DOM TiO$_2$ system was evaluated in terms of degradation of organic pollaunts such as Rhodamine B (RhB) aqueous solution. Rhodamine B, a xanthene dye is widely used as a colorant in textiles and food stuffs, and is also a well-known water tracer fluorescent [42]. It is harmful to human beings and animals, and causes irritation of the skin, eyes and respiratory tract. The carcinogenicity, reproductive and developmental toxicity, neurotoxicity and chronic toxicity toward humans and animals have been experimentally proven [43,44]. During the photocatalytic process, the dye molecules are adsorbed on the surface of the catalysts, where chemical bonds are broken and small organic molecules are released as decomposed products. When the photocatalyst is irradiated in the presence of water hydroxyl radicals OH$^{\cdot}$, as strong oxidant agent, are photogenerated. These reactive species are able to achieve a complete mineralization of organic dyes. Rhodamine B (RhB) is a common dye in the triphenylmethane family, which contains four N-ethyl groups ateither side of the xanthene ring. It has been reported that in the visible-light induced photocatalytic degradation of RhB, as N-ethyl-containing dye, three main steps, namely N-deethylation, cleavageof chromoporme and mineralization of dye, were frequently witnessed [45–47]. At the end of photocatalytic process, the RhB dye is completely mineralized into CO$_2$, H$_2$O [48–53].

In this work, a series of BiVO$_4$/3DOM TiO$_2$ nanocomposites with different compositions have been synthesized. The effect of BiVO$_4$ as visible light sensitizer on the photocatalytic activity has been studied. The BiVO$_4$ content in BiVO$_4$/3DOM TiO$_2$ nanocomposites has been optimized. The charge transfer and interaction between BiVO$_4$ with 3DOM TiO$_2$ have been discussed on the basis of structural, textural, optical and surface characterization. The present contribution will shed some light on the design of optimized photocatalys for dye pollutant aqueous removal.

## 2. Experimental

2.1. Synthesis of BiVO₄/3DOM TiO₂ nanocomposites

The fabrication of BiVO$_4$/3DOM TiO$_2$ nanocomposites was achieved via a hydrothermal strategy, as reported in our previous work [36] in which stoichiometric amounts of Bi(NO$_3$)$_3$·5H$_2$O (Carl Roth, $98%, p.a. ACS) and NH$_4VO_3$ (Carl Roth, $98%, p.a.) were dissolved in a stoichiometric volume of an ethylene glycol–water mixture and stirred for about 10 min until a clear solution was formed. Then, the desired amount of 3DOM TiO$_2$ was added into the solution and sonicated for 15 min. After 1 h stirring, the obtained yellow coloured mixture was transferred into a Teflon-sealed autoclave which was maintained at 160 °C for 24 h. The solid powders were recovered by centrifugation and washed three times with distilled water and absolute ethanol. Finally, the obtained solid was vacuum-dried at 60 °C for 6 h and then calcined at 300 °C for 1 h. Dumbbell-like BiVO$_4$ and 3DOM TiO$_2$ were taken as reference to evaluate the photocatalytic activity of both samples 0.04BiVO$_4$/3DOM TiO$_2$ and 0.08BiVO$_4$/3DOM TiO$_2$, the 0.04 and 0.08 designed the molar ratio Bi:Ti; the synthesized method was detailed in [36]. Herein, three nanocomposites were synthesized with different ratios labeled 0.2BiVO$_4$/3DOM TiO$_2$, 0.4BiVO$_4$/3DOM TiO$_2$ and 0.6BiVO$_4$/3DOM TiO$_2$, respectively.

2.2. Materials characterization

The crystalline structure of the powder samples was characterized by powder X-ray diffraction (XRD) (a PANalytical X'pert Pro with Cu Kα radiation). The morphological properties were analyzed by scanning electron microscopy (SEM) (Jeol JSM-7500F). Part of transmission electron microscopy (TEM) study was performed on a Philips FEI-Tecnai 10 electron microscope with an accelerating voltage of 80 kV. Transmission electron microscopy (TEM), scanning transmission electron microscopy (STEM), and energy dispersive X-ray spectroscopy (EDX) were peformed on a FEI Osiris electron microscope fitted with Super-X windowless EDX dectector system, operated at 200 kV. X-ray photoelectron spectroscopy (XPS) analysis was performed on a K-Alpha^{TM} + X-ray photoelectron spectrometer (XPS). The binding energy for the C (1s) peak at 284.9 eV (relative to adventitious carbon from the XPS instrument itself) was used as a reference. Textural properties of the materials were evaluated via adsorption–desorption of nitrogen at −196 °C using a Micromeritics Tristar 3000 with prior outgassing. The UV–vis absorbance spectra were obtained using a UV–vis spectrophotometer (Perkin Elmer Lambda 35 UV–vis spectrometer fitted with a Labsphere for analysis in diffuse reflectance mode) in the range of 200–750 nm. Photoluminescence properties of the samples were studied by Perkin Elmer LS45 luminescence spectrometry. The photocatalyst podwer has been charged in smple holder supplied by spectrometry manufacturer and then photoluminescence was then recorded.

2.3. Photocatalytic testing

Photocatalytic performances of the as-prepared photocatalysts were measured under visible light irradiation (400–800 nm) using 6 neon lamps of 18 W. The luminous power of each lamp was 1250 lm and the total luminous power was 7500 lm in the photocatalytic reactor. The reaction temperature was maintained at room temperature. We used a very strong ventilation system and the temperature of the photocatalytic reactor is followed to ensure the room temperature of photocatalytic reactor. In each experiment 20 mg of the photocatalyst was placed in 50 mL of a reactant solution with an initial concentration of 10^{-3} M of RhB. The suspension was poured into a quartz tube, inserted into a reactor and stirred in
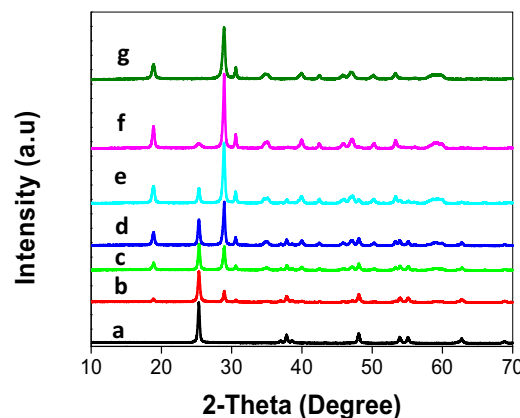
Fig. 1. XRD patterns of 3DOM TiO$_2$ (a), BiVO$_4$/3DOM TiO$_2$ nanocomposites with different mole ratios:(b) 0.04 BiVO$_4$/3DOM TiO$_2$, (c) 0.08BiVO$_4$/3DOM TiO$_2$, (d) 0.2BiVO$_4$/3DOM TiO$_2$, (e) 0.4BiVO$_4$/3DOM TiO$_2$ and (f) 0.6BiVO$_4$/3DOM TiO$_2$ and BiVO$_4$ nanoparticles (g).

the dark for 120 min to ensure adsorption/desorption equilibrium prior to irradiation. During irradiation, 2 mL of the suspension was removed at a given time interval for subsequent RhB concentration analysis.

3. Results and discussions

3.1. Phase composition

XRD patterns of the as-prepared BiVO$_4$/3DOM TiO$_2$ nanocomposites with different BiVO$_4$ content are illustrated in Fig. 1, and compared with those of dumbbell-like BiVO$_4$ nanoparticles and 3DOM TiO$_2$ with an inverse opal structure. The BiVO$_4$ particles (Fig. 1g) exhibit distinctive diffraction peaks, which can be well indexed to monoclinic BiVO$_4$ (JCPDS card No. 14-0688). For pure 3DOM TiO$_2$ particles (Fig. 1a), the diffraction peaks are assigned to the anatase phase, matching very well with JCPDS card No. 21-1272. The diffraction peaks of the 0.04BiVO$_4$/3DOM TiO$_2$ (Fig. 1b), 0.08BiVO$_4$/3DOM TiO$_2$ (Fig. 1c), 0.2BiVO$_4$/3DOM TiO$_2$ (Fig. 1d), 0.4BiVO$_4$/3DOM TiO$_2$ (Fig. 1e) and 0.6BiVO$_4$/3DOM TiO$_2$ (Fig. 1f) nanocomposite photocatalysts, are composed of the characteristic peaks corresponding to monoclinic BiVO$_4$ and anatase TiO$_2$. For all BiVO$_4$-TiO$_2$ heterojunction samples the introduction of BiVO$_4$ nanoparticles did not change the crystal phase and crystallinity of TiO$_2$.

3.2. Morphology

Fig. 2 shows SEM images of the 0.2 BiVO$_4$/3DOM TiO$_2$ sample at different magnification. As can be seen the 0.2 BiVO$_4$/3DOM TiO$_2$ nanocomposite exhibits a dual morphology, spherical-like nanoparticles corresponding to BiVO$_4$, incorporated in the large macropores of 3DOM TiO$_2$. As for the BiVO$_4$ nanoparticles, the average diameter is ranging from 70 to 90 nm. The TiO$_2$ support exhibits a high quality 3DOM inverse opal structure. The underlying layer of pores and porous walls can be clearly observed, indicating that the sample possesses a three-dimensionally well-open, ordered and interconnected macroporous network.

Transmission electron microscopy (TEM) has been used to prove the formation of heterojunctions in the BiVO$_4$/3DOM TiO$_2$ nanocomposite. The low magnification TEM images of the 0.2BVO$_4$/3DOM TiO$_2$ photocatalyst in Fig. 3a confirm the existence of two morphologies: spherical-like BiVO$_4$ nanoparticles embedded in the 3DOM TiO$_2$ support with an interconnected porous structure (Fig. 3b). As can be clearly seen from Fig. 3c, the TiO$_2$
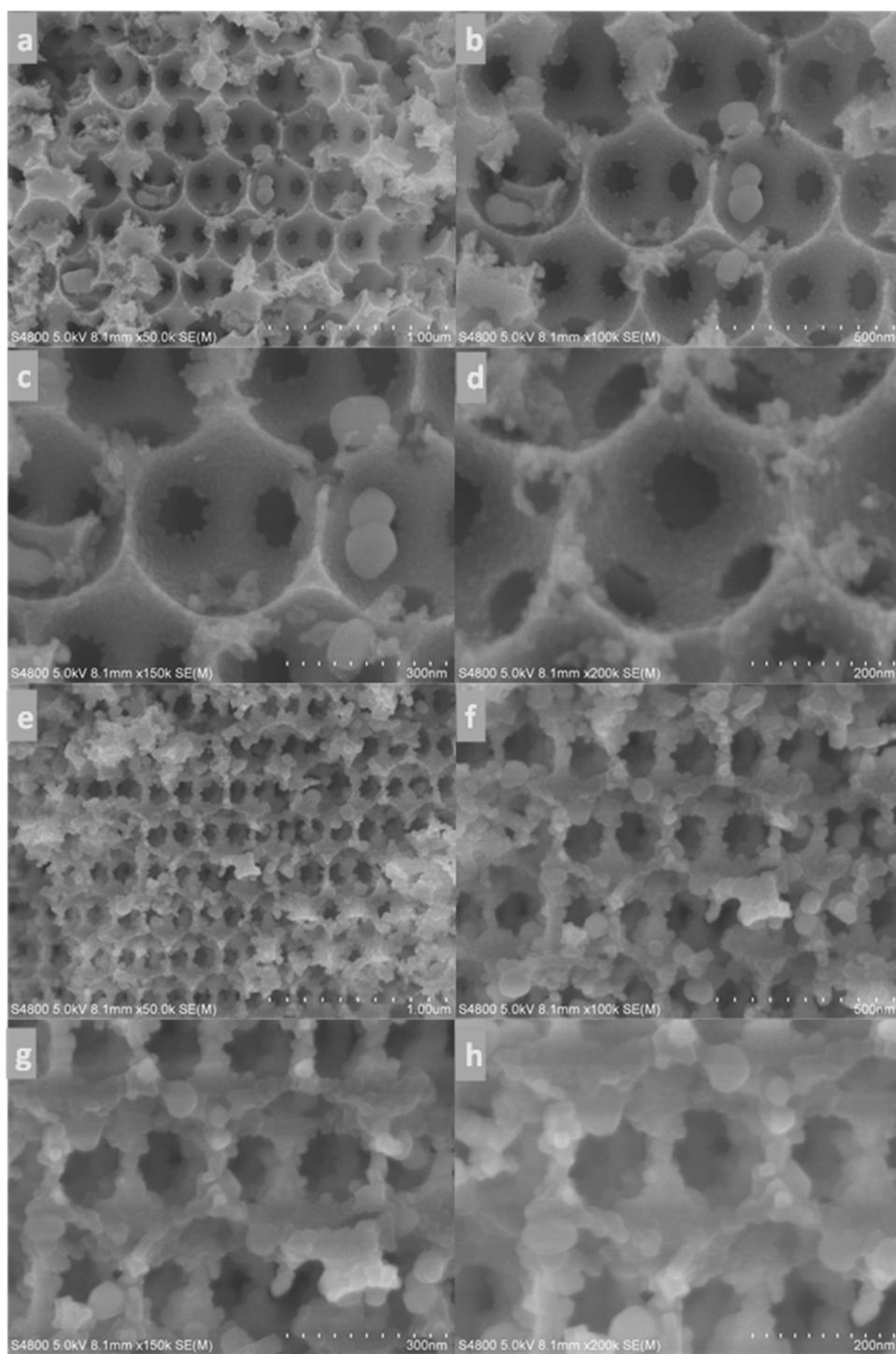
Fig. 2. SEM images of 0.2BiVO$_4$/3DOM TiO$_2$ nanocomposite.

is present as small nanoparticles. The corresponding HRTEM image (Fig. 3d) exhibits two kinds of lattice fringes, one of d = 0.352 nm which matches the (101) crystallographic planes of anatase TiO$_2$, the second of d = 0.312 nm which corresponds to the (130) crystallographic plane of monoclinic BiVO$_4$. It is clear that a heterojunction structure with intimate contact at a nano scale is formed between both semiconductors.

The Z-contrast HAADF-STEM image in Fig. 4a reveals the highly ordered 3DOM TiO$_2$ inverse opal structure with the embedded spherical BiVO$_4$ particles more clearly because the image intensity is approximately proportional to the square of the atomic number (Z^2) and the thickness of the specimen. The higher magnification HAADF-STEM image (Fig. 4b) shows the dispersion of the BiVO$_4$ nanoparticles of 70–90 nm (in good agreement with the SEM image in Fig. 2). The corresponding EDX elemental maps (Fig. 4c–e) show very clearly the highly homogeneous dispersion of the BiVO$_4$ nanoparticles. The enlarged HAADF-STEM image (Fig. 4f) of a small zone (Fig. 4b) and its corresponding EDX elemental maps (Fig. 4g, h and i) indicate the existence of very small nanoparticles of around 2–5 nm of BiVO$_4$ imbeded in the framework of the 3DOM TiO$_2$ structure. The HRTEM of the corresponding zone (Fig. 4k) confirms
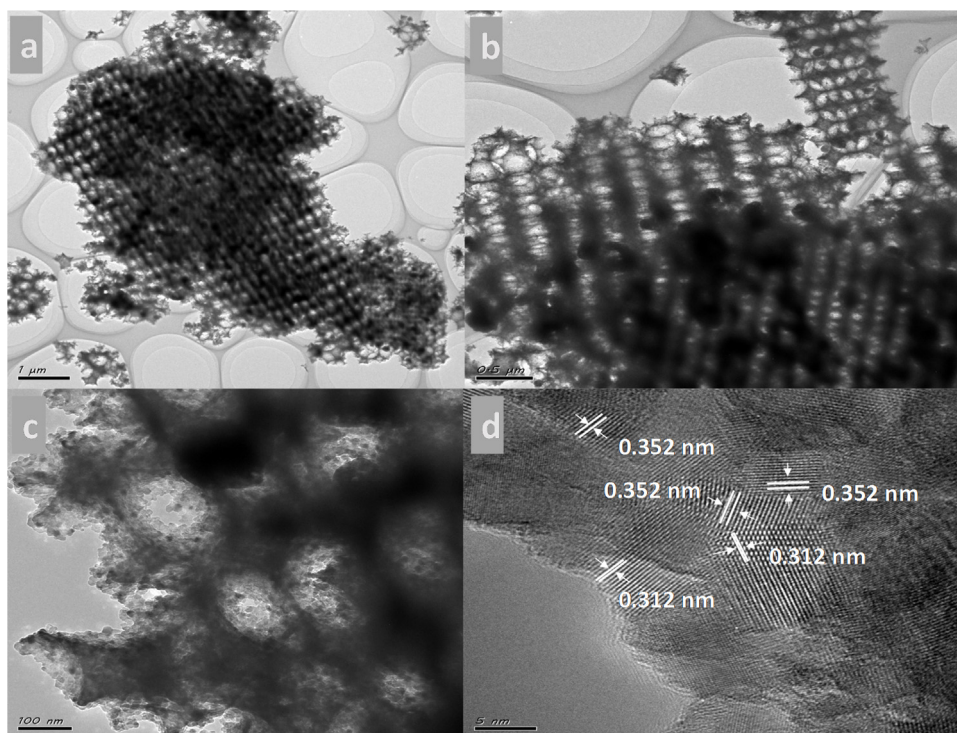
Fig. 3. TEM images (a-c) and HRTEM image (d) of the 0.2BiVO$_4$/3DOM TiO$_2$ nanocomposite.

that BiVO$_4$ nanoparticles are in direct and intimate contact with the TiO$_2$ nanoparticles.

3.3. XPS analysis

The X-ray photoelectron spectroscopy (XPS) was carried out to further determinate the chemical states and the composition of the BiVO$_4$/3DOM TiO$_2$ nanocomposites. For the sake of the clarity, only the results of 0.2BiVO$_4$/3DOM TiO$_2$ are presented and analyzed and compared with pure 3DOM TiO$_2$ and pure BiVO$_4$ nanoparticle photocatalysts. From Fig. 5, four dominate elements (Bi, V, Ti, and O) are found, confirming the presence of BiVO$_4$ and TiO$_2$ in the sample. Fig. 5a shows the Bi 4f spectra of the 0.2 BiVO$_4$/3DOM TiO$_2$ sample compared with that of bare BiVO$_4$. There are two strong peaks at 159 eV and 164.4 eV, which are assigned to Bi 4f7/2 and Bi 4f5/2 and correspond to Bi^{3+} [10,54]. Compared with pure BiVO$_4$ nanoparticles there is a shift of 0.4 eV in the position of Bi 4p7/2 (164 eV) and Bi 4f5/2 (158.6). Two symmetric spectra of V 2p1/2 and V 2p3/2 in the 0.2BiVO$_4$/3DOM TiO$_2$ composite at binding energies of 524.5 and 516.8 eV, respectively (shown in Fig. 5b) are characteristic of V^{5+} ions [55]. Compared with pure BiVO$_4$, a shift of 0.5 eV is observed in the peak position corresponding to V 2p (524.0 for the V 2p1/2 orbit and 516.3 eV for V 2p3/2). In Fig. 5d, the 0.2BiVO$_4$/3DOM TiO$_2$ composite presents two spectra of Ti 2p at 458.1 and 463.8 eV assigned to Ti 2p3/2 and Ti 2p1/2, respectively. The spectrum separation between Ti 2p3/2 and Ti 2p1/2 is 5.7 eV, which stems from the expected oxidation state of Ti^{4+} [56,57]. A shift of 0.7 eV in the peak position of Ti 2p in the 0.2BiVO$_4$/3DOM TiO$_2$ compared with pure TiO$_2$ (458.8 eV and 464.5 eV) indicates that a charge transfer between TiO$_2$ and BiVO$_4$ occurred after the formation of the nanocomposite. The O 1s spectrum is located at 529.1 eV with an asymmetric pattern as shown in Fig. 5e. The primary spectrum indicates the presence of O^{2-} ions, while the additional shoulders at higher energies are assigned to surface OH$^-$ groups and/or chemisorbed H$_2$O [58]. For the BiVO$_4$ and TiO$_2$ samples, the O1s peaks are located at 529.4 and 530 eV, respectively. As we can

note, the Bi 4f, V 2p, Ti 2p and O 1s peaks in the 0.2BiVO$_4$/3DOM TiO$_2$ show a significant shift confirming that a significant interaction exists between the two coupled semiconductors. As for the 0.08BiVO$_4$/3DOM TiO$_2$ nanocomposite, as detailed in [36] the shift values of the Bi4f, V2p, Ti2p and O1s elements were found to be: 0.3, 0.3, 0.6 and 0.2, respectively.

3.4. Textural properties

The N$_2$ adsorption–desorption isotherms and pore-size distributions curves of the samples are illustrated in Fig. 5. The obvious macroporous structure enables each of the 3DOM TiO$_2$, 0.2BiVO$_4$/3DOM TiO$_2$, 0.4 BiVO$_4$/3DOM TiO$_2$ and 0.6 BiVO$_4$/3DOM TiO$_2$ samples to exhibit a type II isotherm, according to IUPAC classification, with a type H3 hysteresis loop in the relative pressure range of 0.9–1.0. BET specific surface areas of pure BiVO$_4$ nanoparticles, 3DOM TiO$_2$ inverse opal structure and BiVO$_4$/3DOM TiO$_2$ nanocomposites with different molar ratios are shown in Table 1.

The 3DOM TiO$_2$ sample shows a higher surface area than the composite samples with a value of 30 m^2/g. It should be noted that large surface areas of the photocatalysts play an important role in enhancing photocatalytic activities by favoring the adsorption of small dye molecules at the active surface of these samples. However, it decreases significantly after the introduction of BiVO$_4$ nanoparticles to about 15 m^2/g for 0.2BiVO$_4$/3DOM TiO$_2$, 12 m^2/g for 0.4BiVO$_4$/3DOM TiO$_2$ and 7 m^2/g for 0.6BiVO$_4$/3DOM TiO$_2$. The BET surface area for 0.04BiVO$_4$/3DOM TiO$_2$ and 0.08BiVO$_4$/3DOM TiO$_2$ nanocomposites and BiVO$_4$ nanoparticles is found to be 25, 17 and 4 m^2/g, respectively [46]. Moreover, the pore-size distribution calculated by the desorption branch of isotherm for all samples, as shown by the inset curves in Fig. 6, shows a narrow pore-size distribution ranging from 2.3 to 9 nm, due to aggregations of the nanoparticles. The calculated BET surface area for all samples are summarized in Fig. 7 and it confirms that there is a significant decrease in surface area when increasing the amount of BiVO$_4$ nanoparticles.
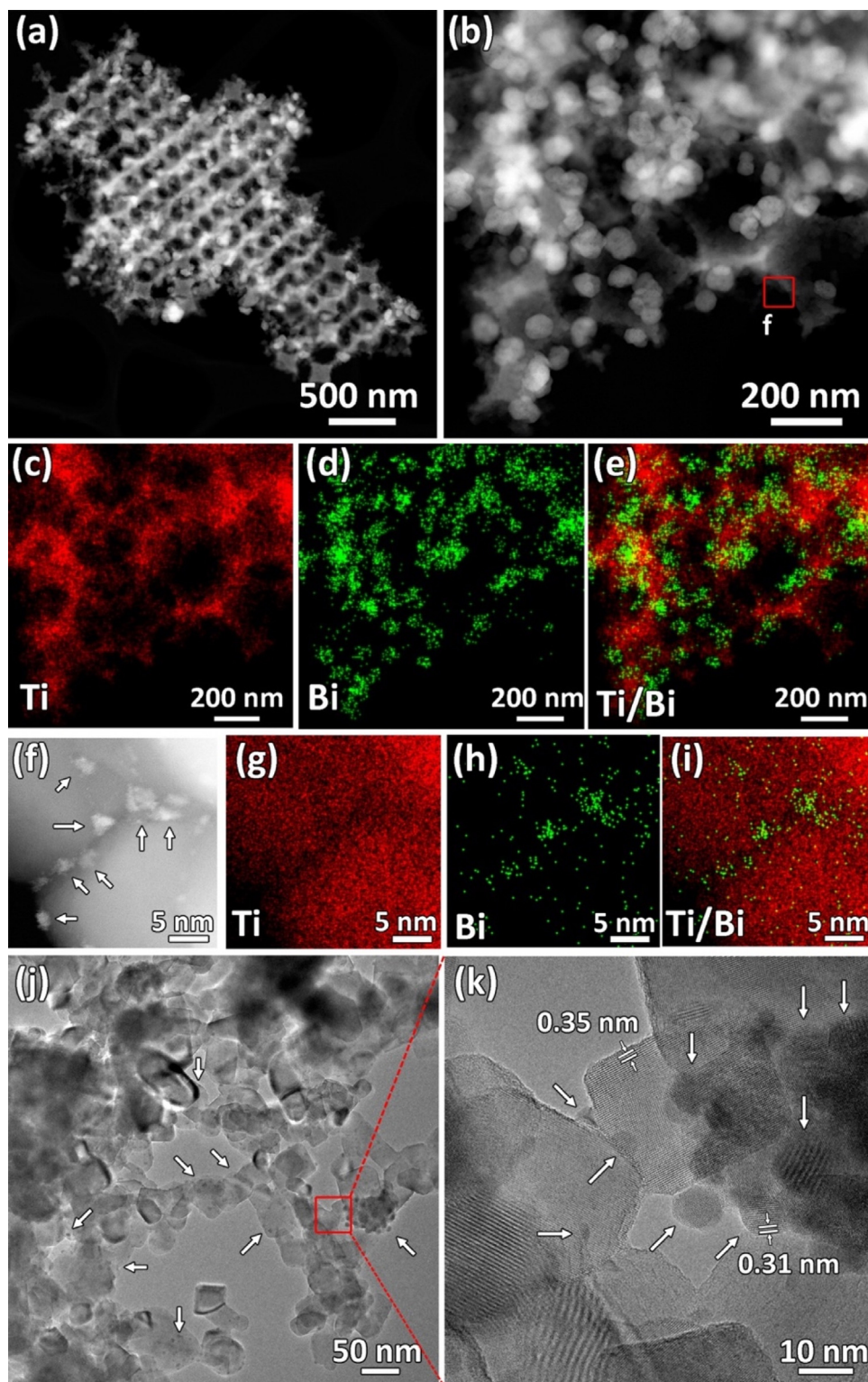
Fig. 4. (a, b, f) HAADF-STEM images at different magnification, (c-e) corresponding EDX elemental maps of the whole area of (b). (g–i) corresponding EDX elemental maps of the whole area of (f), (i) TEM image, (k) HRTEM image of the area indicated in (j) with a red box. The $BiVO_4$ nanoparticles are indicated by white arrows. (For interpretation of the references to colour in this figure legend, the reader is referred to the web version of this article.)

3.5. Optical properties

The optical absorption property of the semiconductor is a key factor in affecting the photocatalytic performance [59]. Fig. 8 shows the UV–vis absorption spectra of the as-prepared samples. The pure 3DOM TiO_2 (spectrum a) exhibits photoresponsiveness in the UV region (wavelength below 395 nm) because of its wide energy band gap (3.2 eV). In addition, the absorption edge of $BiVO_4$ nanoparticles (spectrum e), estimated at 525 nm, is assigned to the band transition from the Bi 6s orbital to a V 3d conduction band. As can be clearly seen, the absorption in the visible light range of $BiVO_4$/3DOM TiO_2 samples remarkably increases with
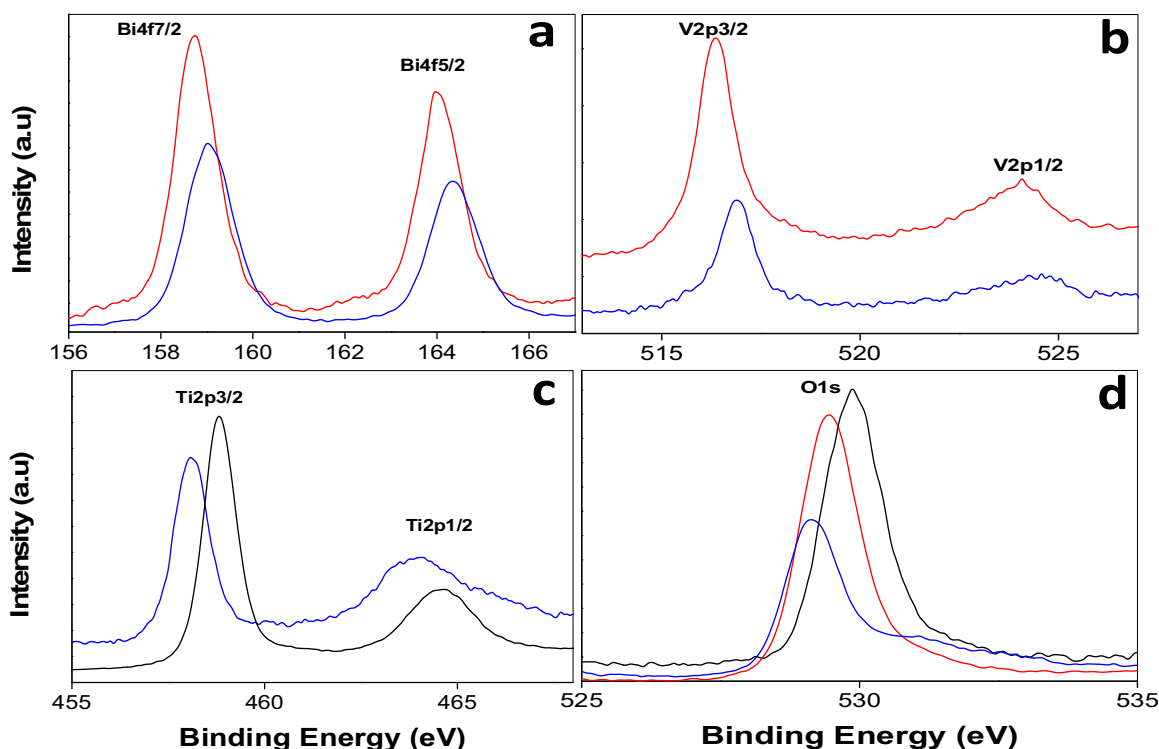
Fig. 5. XPS spectra of (a) Bi4f, (b) V2p, (c) Ti2p and (d) O1s for 0.2BiVO$_4$/3DOM TiO$_2$ (blue line) compared with pure BiVO$_4$ nanoparticles (red line) and 3DOM TiO$_2$ inverse opal structure (black line). (For interpretation of the references to colour in this figure legend, the reader is referred to the web version of this article.)

Table 1
BET specific surface area, average pore diameter and pore volume of 3DOM TiO$_2$, BiVO$_4$ nanoparticles and BiVO$_4$/3DOM TiO$_2$ heterojunction photocatalysts.

Materials	$S_{BET}(m^2\,g^{-1})$	Pore size(nm)	Pore volume(cm^3 g^{-1})
3DOM TiO$_2$	30	2.3	0.0062
0.04BiVO$_4$/3DOM TiO$_2$	25	2.4, 8	0.0028
0.08BiVO$_4$/3DOM TiO$_2$	17	2.5, 7	0.0022
0.2BiVO$_4$/3DOM TiO$_2$	15	2.1, 5	0.004
0.4BiVO$_4$/3DOM TiO$_2$	11	2.2, 6	0.0032
0.6BiVO$_4$/3DOM TiO$_2$	7	2.3, 9	0.0027
BiVO$_4$	4	23	0.00032

the increase of BiVO$_4$ nanoparticles. The absorption edge of the 0.2BiVO$_4$/3DOM TiO$_2$, 0.4BiVO$_4$/3DOM TiO$_2$ and 0.6BiVO$_4$/3DOM TiO$_2$ nanocomposites (spectra b-d) are quite close to that of BiVO$_4$ nanoparticles and their absorption intensities were obviously higher than that of 3DOM TiO$_2$. Compared with 0.04BiVO$_4$/3DOM TiO$_2$ and 0.08BiVO$_4$/3DOM TiO$_2$ nanocomposites, as shown in [36], the absorption edge is more shifted to the visible range with increasing the BiVO$_4$ amount in the nanocomposite.

Moreover, the energy band structures of a semiconductor stay important in determining its photocatalytic activity. The relation between the absorbance and incident photon energy $h\nu$ can be described by the following equation:

$$(\alpha h\nu) = A(h\nu - Eg)^{1/2}$$

where α, Eg, h, ν and A represent the absorption coefficient, the band-gap energy, the Planck constant, the incident light frequency and a constant, respectively. The band-gap energy can therefore be estimated from the intercept of the plots of $(\alpha h\nu)^{1/2}$ versus $(h\nu)$ as illustrated in Fig. 7(b). The corresponding band gap energies are found to be 2.38, 3.14, 2.39, 2.4 and 2.43 eV for BiVO$_4$ nanoparticles, 3DOM TiO$_2$ inverse opal structure, 0.2 BiVO$_4$/3DOM TiO$_2$, 0.4 BiVO$_4$/3DOM TiO$_2$ and 0.6 BiVO$_4$/3DOM TiO$_2$ nanocomposites, respectively. The estimated band gap energies of 0.04 BiVO$_4$/3DOM

TiO$_2$ and 0.08 BiVO$_4$/3DOM TiO$_2$ photocatalysts were found to be 2.44 and 2.41 eV.

The photoluminescence (PL) is a facile technique to study the photochemical properties of semiconductor materials, where the PL emission mainly originates from the recombination of the excited electrons and holes [60]. Fig. 9 presents the PL spectra of the 3DOM TiO$_2$ and BiVO$_4$/3DOM TiO$_2$ samples. The pure TiO$_2$ inverse opal structure (spectrum a) gives a strong PL signal located at 420 nm mainly resulting from band edge free excitons and four obvious PL peaks at about 442, 457, 485 and 527 nm, respectively, possibly resulting from binding excitons [61,62]. It has been reported that a higher peak intensity indicates a larger probability of charge carrier recombination [63]. Semiconductors with lower PL intensities usually exhibit higher photocatalytic activity due to a lower charge recombination rate.

The highest photoluminescence intensity is observed for 3DOM TiO$_2$, indicating its high photogenerated electron–hole recombination efficiency which could lead to a reduced photocatalytic activity. For all BiVO$_4$/3DOM TiO$_2$ samples (spectra b-f), the PL spectrum shows a strong emission at 525 nm which originates from the recombination of the hole formed from the hybrid orbitals of Bi 6s and O 2p (valence band VB) and the electron generated from the V 3d orbitals (conduction band CB) [47]. Compared with the inverse opal structure TiO$_2$, the PL emission decreases signif-
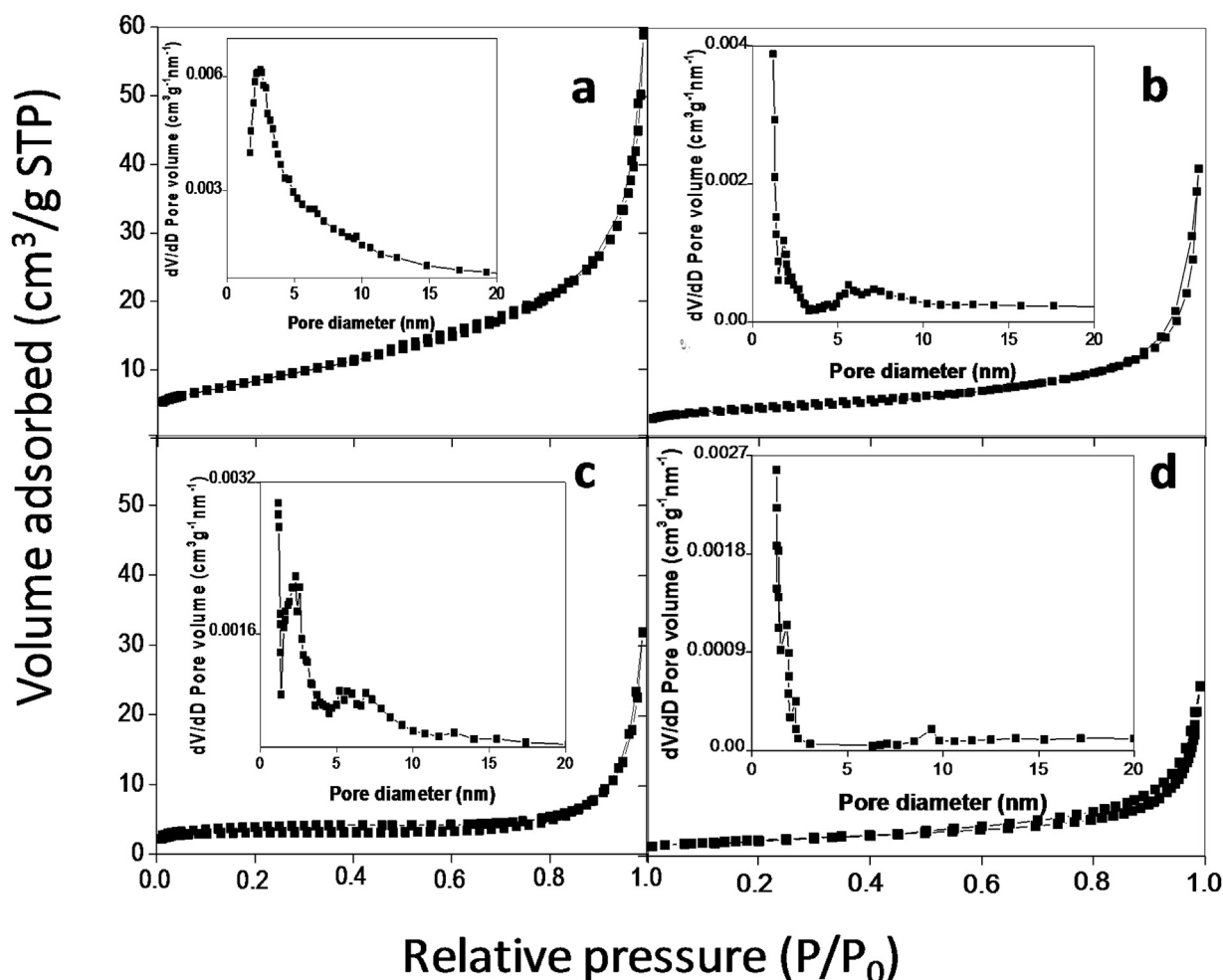
Fig. 6. Nitrogen adsorption-desorption isotherms and pore size distribution curve (inset) of (a) 3DOM TiO_2, (b) 0.2$BiVO_4$/3DOM TiO_2, (c) 0.4$BiVO_4$/3DOM TiO_2 and (d) 0.6$BiVO_4$/3DOM TiO_2 nanocomposites photocatalysts.
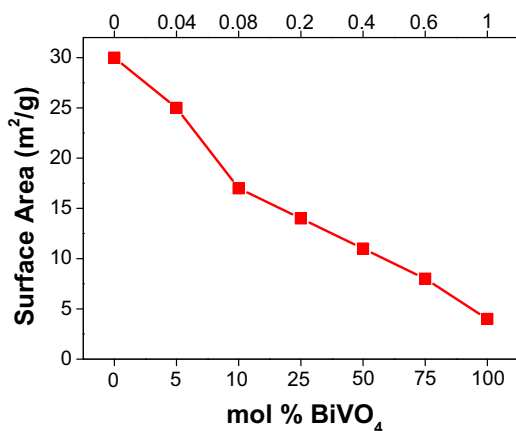
**Fig. 7.** BET surface area variation with increasing molar ratios.

icantly for all nanocomposites. The PL intensity is progressively reduced with increasing $BiVO_4$ amount in the 3DOM TiO_2 IO structure. This behavior shows that efficient charge or energy transfer occurs at the $BiVO_4$/TiO_2 heterojunction interface. The PL intensity is lower as the percentage of $BiVO_4$ increases from 0.04 to 0.2. In particular, the 0.2 $BiVO_4$/TiO_2 (spectrum f) shows the lowest PL intensity as compared to other samples. The emission peak at 420 nm almost disappears, indicating the inhibition of an intrinsic radiative recombination path. Accordingly, it is inferred that the recombination rate between photogenerated holes and electrons is significantly reduced in the nanocomposite. In other words, the formation of heterojunction between $BiVO_4$ and TiO_2 is helpful to improve the transfer characteristic of photogenerated carries and to enhance the photocatalytic activity. However, as can be noted in Fig. 9 (spectra d and e) the 0.4$BiVO_4$/3DOM TiO_2 and 0.6 $BiVO_4$/3DOM TiO_2 nanocomposites show a higher PL intensity compared with that of the 0.2 $BiVO_4$/3DOM TiO_2 nanocomposite, indicating a high recombination rate. After increasing the $BiVO_4$ content in the nanocomposite it becomes even more important than the 3DOM TiO_2 amount, as shown by the XRD results; the photogenerated electron-hole charge carriers are accumulated in the $BiVO_4$ sensitizer and the recombination rate increases significantly.

3.6. Photocatalytic performance

The photocatalytic performance of the as-prepared samples has been examined in terms of degradation of RhB in an aqueous solution under visible-light irradiation. In our previous work the 3DOM TiO_2 inverse opal structure, dumbbell-like $BiVO_4$ nanoparticles, 0.04 $BiVO_4$/3DOM TiO_2 and 0.08 $BiVO_4$/3DOM TiO_2 nanocomposite photocatalysts were studied [36]. Herein the photocatalytic activity of three new nanocomposites labeled 0.2 $BiVO_4$/3DOM TiO_2, 0.4$BiVO_4$/3DOM TiO_2 and 0.6$BiVO_4$/3DOM TiO_2 was measured under the same conditions. All results are compared, as shown in Fig. 10, in order to evaluate the variation of the photocatalytic effi-
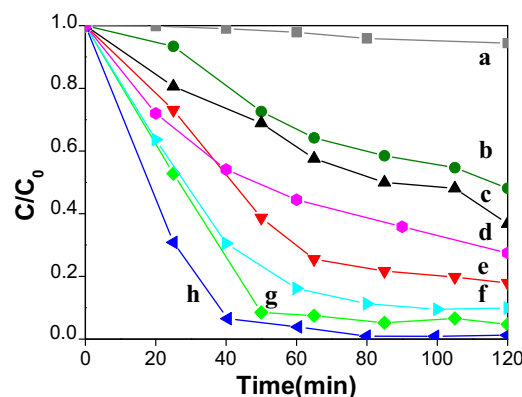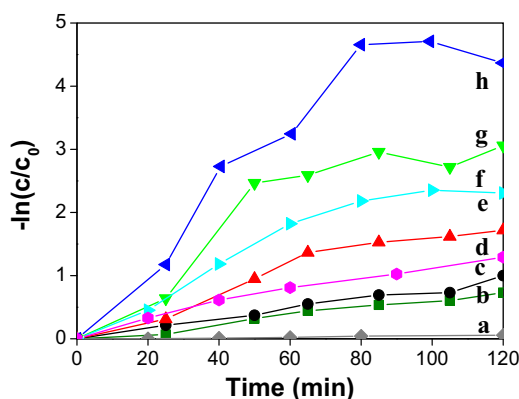
Fig. 10. Photocatalytic degradation of RhB over the as-prepared samples under visible-light irradiation: (a) Blank, (b) BiVO$_4$ nanoparticles (c) 3DOM TiO$_2$, (d) 0.6BiVO$_4$/3DOM TiO$_2$, (e) 0.04BiVO$_4$/3DOM TiO$_2$, (f) 0.4BiVO$_4$/3DOM TiO$_2$, (g) 0.08BiVO$_4$/3DOM TiO$_2$ and (h) 0.2BiVO$_4$/3DOM TiO$_2$.
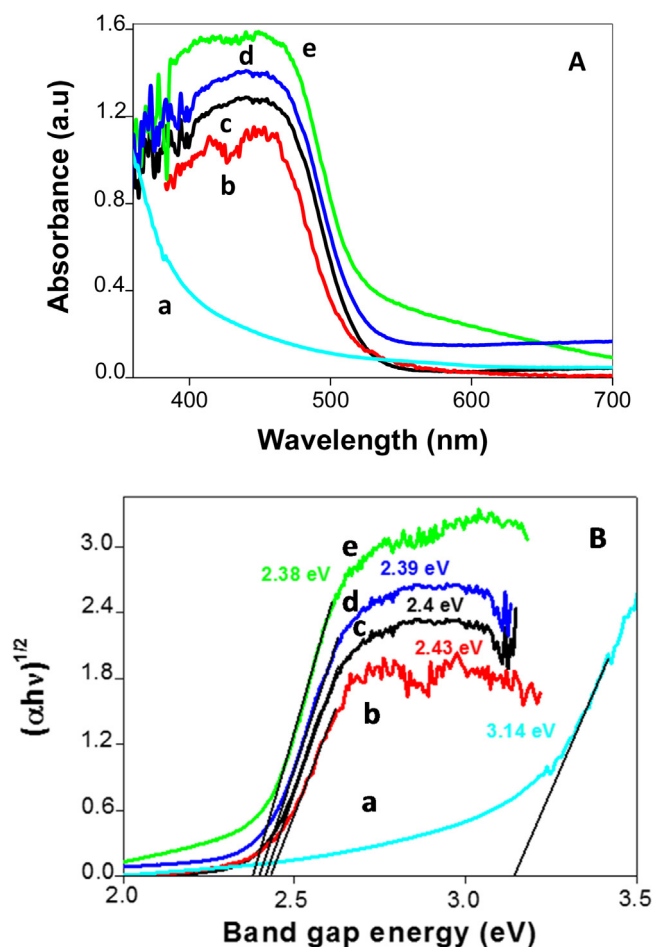
Fig. 8. (A) UV–vis diffuse absorption spectra and (B) the plots of $(\alpha h\nu)^{1/2}$ versus photon energy (hν) of (a) pure 3DOM TiO$_2$, (b) 0.2BiVO$_4$/3DOM TiO$_2$, (c) 0.4BiVO$_4$/3DOM TiO$_2$ and (e) 0.6BiVO$_4$/3DOM TiO$_2$ nanocomposites and (e) pure BiVO$_4$ nanoparticles.
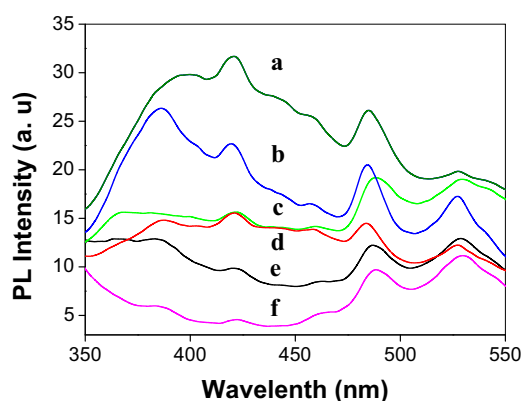
Fig. 9. Photoluminescence spectra of (a) pure 3 DOM TiO$_2$, (b) 0.08BiVO$_4$/3DOM TiO$_2$, (c) 0.04BiVO$_4$/3DOM TiO$_2$, (d) 0.6BiVO$_4$/3DOM TiO$_2$, (e) 0.4BiVO$_4$/3DOM TiO$_2$ and (f) 0.2BiVO$_4$/3DOM TiO$_2$ nanocomposites samples.

ciency by increasing the amount of the BiVO$_4$ nanoparticles in the nanocomposite.

A Blank experiment (curve a) in the absence of any photocatalyst shows no significant change in the RhB concentration. As can be seen the photodegradation rate for all samples increases as the reaction time increases. The dumbbell-like BiVO$_4$ (curve b) shows a very poor photocatalytic activity, only 22% of RhB being degraded in 120 min which can be related to the intrinsic properties of the BiVO$_4$ samples, such as the very poor adsorptive performance towards

organic dye molecules and the inefficient migration of photogenerated electron–hole pairs to the surface for photocatalytic reactions. Thus BiVO$_4$ nanoparticles exhibit a very low activity despite its absorption in the visible light related to its narrow band gap energy of 2.4 eV. TiO$_2$ has a large electronic band gap and it absorbs only in the UV range, however the photocatalytic performance is higher than that of BiVO$_4$ nanoparticles but it is still relatively poor, only 28% being degraded in 120 min (curve c). The reason is probably related to the 3DOM TiO$_2$ IO structure which can provide a more active surface area, more contact area and an increased mass transfer because of its highly accessible 3D porosity.

After the introduction of BiVO$_4$ nanoparticles, the photocatalytic activity is tremendously improved compared with the original 3DOM TiO$_2$ inverse opal structure and pure BiVO$_4$ nanoparticles. The photocatalytic performance of the coupled BiVO$_4$/3DOM TiO$_2$ nanocomposite increases and then decreases after reaching a maximum value as the proportion of BiVO$_4$ increases from 0.04 to 0.6. The 0.2BiVO$_4$/3DOM TiO$_2$ (curve h) exhibits the highest photocatalytic activity, and about 100% of RhB is photodegraded in the aqueous solution after visible-light irradiation for 80 min. For the 0.04BiVO$_4$/3DOM TiO$_2$ (curve e), 0.08BiVO$_4$/3DOM TiO$_2$ (curve g), 0.4BiVO$_4$/3DOM TiO$_2$ (curve f) and 0.6 BiVO$_4$/3DOM TiO$_2$ (curve d), the conversion rate of RhB is about 80%, 95%, 90% and 85%, respectively. From the photodegradation rate of RhB, it can be inferred that the order of the photocatalytic activity is:

$$0.2BiVO_4/3DOMTiO_2 > 0.08BiVO_4/3DOMTiO_2$$
$$> 0.4BiVO_4/3DOMTiO_2 > 0.04BiVO_4/3DOMTiO_2$$
$$> 0.0.6BiVO_4/3DOMTiO_2 > 3DOMTiO_2 > BiVO_4$$

The enhanced photocatalytic activity of 0.2BiVO$_4$/3DOM TiO$_2$ may originate from the interfacial transfer of electrons and holes as observed by PL and XPS. The formation of a heterojunction structure between BiVO$_4$ and 3DOM TiO$_2$ effectively promotes the separation of photogenerated charge carriers, due to the suitable band alignment between the coupled semiconductors, and extends the absorption wavelength to the visible region. The lifetime of the charge carriers is increased and thus the recombination of electron–hole pairs can be inhibited and the photogenerated high energy can be easily transferred from the BiOV$_4$ to 3DOM TiO$_2$ under the internal field induced by the electronic band structure. Thus, the electrons and holes have more opportunities to participate in reduction and oxidation reactions for the degradation of the organic dye on their surface which results in an increase of the photocatalytic efficiency under visible-light irradiation. More-

Fig. 11. Kinetic curves of RhB photocatalytic degradation over different samples: (a) Blank, (b) $BiVO_4$ nanoparticles (c) 3DOM TiO_2, (d) $0.6BiVO_4$/3DOM TiO_2, (e) $0.04BiVO_4$/3DOM TiO_2, (f) $0.4BiVO_4$/3DOM TiO_2, (g) $0.08BiVO_4$/3DOM TiO_2 and (h) $0.2BiVO_4$/3DOM TiO_2.
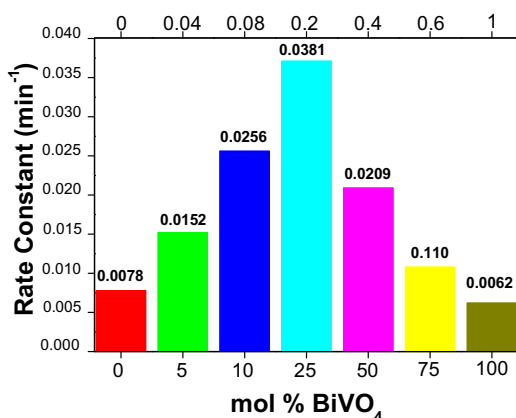

Fig. 12. Variation of the reaction constant with different molar ratios.

over, the 3DOM inverse opal structure with interconnected pores and a high surface area could provide more active sites and more contact surface. As the amount of $BiVO_4$ nanoparticles increases, the sensitization effect increases; more electrons and holes are photogenerated and will participate in the oxidation/reduction process and an improved photocatalytic effect is found. However, the photocatalytic performance reaches a maximum for 0.2 $BiVO_4$/3DOM TiO_2; after that, it decreases with an increase of the amount of $BiVO_4$ nanoparticles in the nanocomposite. Two reasons could account for the low visible light photocatalytic activity of the 0.4 $BiVO_4$/3DOM TiO_2 and 0.6 $BiVO_4$/3DOM TiO_2 nanocomposites compared with that of 0.2 $BiVO_4$/3DOM TiO_2. First, the photogenerated electron/holes are accumulated at the surface of the $BiVO_4$ nanoparticles since the transfer of electrons to 3DOM TiO_2 is reduced due to the decreased TiO_2 amount, the recombination rate thus increases as shown by the PL spectra. The PL intensity is more important for the 0.4 $BiVO_4$/3DOM TiO_2 and 0.6 $BiVO_4$/3DOM TiO_2, respectively, compared with that of 0.2 $BiVO_4$/3DOM TiO_2 photocatalyst, indicating their high recombination rate. Second, some of the photogenerated electrons can be transferred to TiO_2 and participate in the reduction process. However the interfacial charge process is limited by two factors: the low amount of 3DOM TiO_2 as confirmed by XRD analysis and the decrease of the surface area after increasing the amount of $BiVO_4$ nanoparticles as shown by the BET results. As known, the 3DOM photonic structure of TiO_2 with its 3D open meso-macroporosity and large surface area can facilate the diffusion and high accessibility of the dye molecules to the active sites and offer enhanced light propagation owing to multiple scattering and slow photon effect. Moreover, the inverse opal structure of TiO_2 with an open interconnected porous network facilitates the separation of the electron-hole pairs, which might generate more radical species with a strong oxidation capability for dye degradation. For the 0.4 $BiVO_4$/3DOM TiO_2 and 0.6 $BiVO_4$/3DOM TiO_2 nanocomposites, as the amounts of 3DOM TiO_2 decrease compared with $BiVO_4$ nanoparticles the surface area decreases significantly. The adsorptive performance of $BiVO_4$/3DOM TiO_2 nanocomposites become very poor and the dye molecules diffusion is reduced. These factors are unfavorable for photocatalysis.

A pseudo-first-order kinetic model was employed to fit the degradation data by using the linear transformation: $\ln(C_0/C_t) = kt$ (k is the kinetic constant, while C_0 and C_t are the initial concentration and the concentration of RhB during the reaction time, respectively). The kinetics of RhB degradation over the $BiVO_4$/3DOM TiO_2 nanocomposites with different composition, pure 3DOM TiO_2 inverse opal structure and $BiVO_4$ nanoparti-
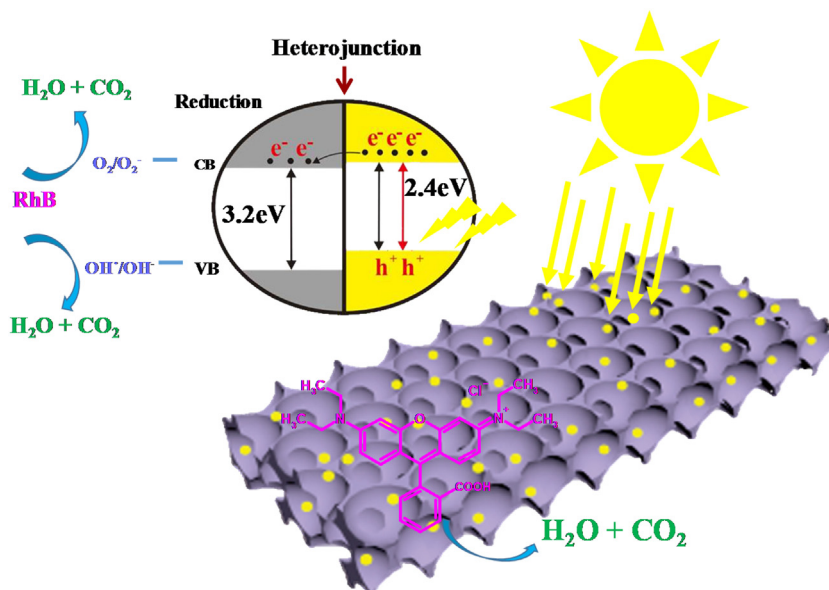
Fig. 13. Schematic representation of energy band diagram and charge transfer process in the $BiVO_4$@3DOM TiO_2 nanocomposite.

cles are presented in Fig. 11. The kinetic constants of the pure $BiVO_4$ nanoparticles, pure 3DOM TiO_2, 0.04$BiVO_4$/3DOM TiO_2, 0.08$BiVO_4$/3DOM TiO_2, 0.2$BiVO_4$/3DOM TiO_2, 0.4$BiVO_4$/3DOM TiO_2 and 0.6$BiVO_4$/3DOM TiO_2 nanocomposites photocatalysts are 0.0062, 0.0078, 0.0152, 0.0256, 0.0381, 0.0209 and 0.0110, respectively, as represented by the histogram in Fig. 12.

As can be seen, the photocatalytic efficiency of the $BiVO_4$/3DOM TiO_2 nanocomposites increases significantly with the amount of $BiVO_4$ nanoparticles to reach a maximum for 0.2 $BiVO_4$/3DOM TiO_2. As we explained in the discussion above, the enhanced photocatalytic activity of the 0.2$BiVO_4$/3DOM TiO_2 nanocomposite is attributed to the synergy of the structural effect in which 3DOM structures with an open interconnected porous network facilitate the diffusion of molecules and offer a larger surface area and the formation of $BiVO_4$/TiO_2 heterojunctions. This effect is favorable for photocatalysis and the interfacial charge transfer, which may lead to an even higher quantum efficiency, supplying more photogenerated electrons in photocatalytic reactions. Moreover, $BiVO_4$ nanoparticles act as light sensitizer leading to visible light absorbing materials and more electron and hole charge carriers are photogenerated. The schematic representation of energy band diagram and charge transfer process in $BiVO_4$/3DOM TiO_2 nanocomposites are given in Fig. 13. When the $BiVO_4$/3DOM TiO_2 nanocomposite photocatalyst is irradiated using visible light (>400 nm), electrons in the valence band (VB) of the $BiVO_4$ nanoparticles are excited to the conduction band (CB), creating holes in the VB. Because the CB edge potential of $BiVO_4$ is more negative than that of TiO_2, the photogenerated electrons of $BiVO_4$ tend to migrate to the CB of TiO_2. The photogenerated holes, which have oxidizing power, are more favorable to react with adsorbed H_2O to produce reactive $^\bullet OH$ radicals. The photogenerated electrons are good reductants, which can be captured by the adsorbed O_2 molecules at the surface of the catalyst and reduce them to $O^{\bullet-}_2$ radicals. These radicals are the main active species to react with the RhB molecules adsorbed at the surface of the nanocomposite during the degradation process. Therefore, the charge transfer between the coupled semiconductors is very beneficial for promoting the photocatalytic activity. The formation of heterojunctions affects the charge separation properties of the composite photocatalyst; the different band gap positions of $BiVO_4$ and TiO_2 allow the visible light photogenerated electrons to flow from the CB of $BiVO_4$ into the CB of TiO_2 so that the recombination of electron-hole (e-h) pairs is suppressed and thus the quantum efficiency is enhanced. As a result, a higher photocatalytic oxidation activity is achieved for the $BiVO_4$/3DOM TiO_2 composite. However, when the proportion of $BiVO_4$ in nanocomposites is higher than 25 mol%, the photogenerated electrons will remain at the surface of $BiVO_4$ and can not be efficiently transferred to TiO_2 as indicated in Fig. 13 due to too low amount of TiO_2 in nanocomposites, leading to high recombination rate of electrons-holes and the highly reduced photocatalytic activity. The amount of $BiVO_4$ as highly efficient visible light sensitizer should be carefully controlled to develop a highly active photocatalyst for dye pollutants degradation.

4. Conclusion

The introduction of $BiVO_4$ nanoparticles was found to extend the spectral response of TiO_2 from the UV to the visible region and to enhance significantly the photocatalytic efficiency towards the degradation of RhB under visible-light irradiation. $BiVO_4$ nanoparticles in the 3DOM TiO_2 inverse opal structure act as a very significant sensitizer to absorb visible light and to transfer efficiently high energy electrons to TiO_2. The formation of heterojunction between $BiVO_4$ and 3DOM TiO_2 induces a more efficient separation of excess charge carriers and retards the recombina-

tion of charge pairs, thereby facilitating the interparticle electron transfer at the $BiVO_4$/3DOM TiO_2 interfaces. The phtotcatalytic activity depends on the amount of $BiVO_4$ in nanocomposites. The photocatalytic performance increases to reach a maximum for the 0.2 $BiVO_4$/3DOM TiO_2. From this value on, as the $BiVO_4$ content increases, the reaction rate decreases. This behavior can be attributed to: 1) the photogenerated electron/holes which are accumulated at the surface of the $BiVO_4$ nanoparticles, leading to easy recombination of photogenerated electron/holes as the $BiVO_4$ amount increases, 2) the low amount of 3DOM TiO_2 resulting in the reduction of surface area of nanocomposites and 3) the poor adsorptive properties of the $BiVO_4$ nanoparticles.

References

[1] Q. Liu, J. He, T. Yao, Z. Sun, W. Cheng, S. He, Y. Xie, Y. Peng, H. Cheng, Y. Sun, Nat. Commun. (2014) 5.
[2] H. Li, Y. Zhou, W. Tu, J. Ye, Z. Zou, Adv. Funct. Mater. 25 (2015) 998–1013.
[3] Q. Li, X. Li, S. Wageh, A. Al-Ghamdi, J. Yu, Adv. Energy Mater. (2015) 5.
[4] H. Tong, S. Ouyang, Y. Bi, N. Umezawa, M. Oshikiri, J. Ye, Adv. Mater. 24 (2012) 229–251.
[5] Y.W. Cheng, R.C.Y. Chan, P.K. Wong, Water Res. 41 (2007) 842–852.
[6] J.H. Park, S. Kim, A.J. Bard, Nano Lett. 6 (2006) 24–28.
[7] M. Ksibi, S. Rossignol, J.M. Tatibouët, C. Trapalis, Mater. Lett. 62 (2008) 4204–4206.
[8] L.G. Devi, N. Kottam, S.G. Kumar, J. Phys. Chem. C 113 (2009) 15593–15601.
[9] H. Cheng, B. Huang, Y. Dai, Nanoscale 6 (2014) 2009–2026.
[10] Y. Huang, B. Long, H. Li, M.S. Balogun, Z. Rui, Y. Tong, H. Ji, Adv. Mater. Interfaces (2015) 2.
[11] M. Guan, C. Xiao, J. Zhang, S. Fan, R. An, Q. Cheng, J. Xie, M. Zhou, B. Ye, Y. Xie, J. Am. Chem. Soc. 135 (2013) 10411–10417.
[12] Y. Ma, Y. Jia, Z. Jiao, M. Yang, Y. Qi, Y. Bi, Chem. Commun. 51 (2015) 6655–6658.
[13] X. Chang, T. Wang, P. Zhang, J. Zhang, A. Li, J. Gong, J. Am. Chem. Soc. 137 (2015) 8356–8359.
[14] L. Ye, J. Liu, C. Gong, L. Tian, T. Peng, L. Zan, ACS Catal. 2 (2012) 1677–1683.
[15] G. Liu, T. Wang, S. Ouyang, L. Liu, H. Jiang, Q. Yu, T. Kako, J. Ye, J. Mater. Chem. A 3 (2015) 8123–8132.
[16] A. Kudo, K. Ueda, H. Kato, I. Mikami, Catal. Lett. 53 (1998) 229–230.
[17] A. Kudo, K. Omori, H. Kato, J. Am. Chem. Soc. 121 (1999) 1459–11467.
[18] S. Kohtani, M. Koshiko, A. Kudo, K. Tokumura, Y. Ishigak, A. Toriba, K. Hayakawa, R. Nakagaki, Appl. Catal. B 46 (2003) 573–586.

[19] S. Kohtani, J. Hiro, N. Yamamoto, A. Kudo, K. Tokumura, R. Nakagaki, Catal. Commun. 6 (2005) 185–189.
[20] K. Sayama, A. Nomura, Z. Zou, R. Abe, Y. Abe, H. Arakawa, Chem. Commun. 9 (2003) 2908–2909.
[21] X. Zhang, Z. Ai, F. Jia, L. Zhang, X. Fan, Z. Zou, Mater. Chem. Phys. 103 (2007) 162–167.
[22] H.T. Yu, X. Quan, S. Chen, H.M. Zhao, J. Phys. Chem. C 111 (2007) 12987.
[23] H. Zhang, X.J. Lv, Y.M. Li, Y. Wang, J.H. Li, ACS Nano. 4 (2010) 380.
[24] H. Huang, S. Wang, Y. Zhang, P.K. Chu, RSC Adv. 4 (2014) 41219.
[25] S.B. Rawal, S. Bera, D. Lee, D.J. Jang, W.I. Lee, Catal. Sci. Technol. 3 (2013) 1822.
[26] S. Obregon, S.W. Lee, G. Colon, Dalton Trans. 43 (2014) 311–316.
[27] B. Cao, J. Peng, Y.Y, J. Cluster Sci. 24 (2013) 771–785.
[28] L. Zhang, G. Tan, S. Wei, H. Ren, A. Xia, Y. Luo, Ceram. Int. 39 (2013) 8597–8604.
[29] Y. Hu, D. Li, Y. Zheng, W. Chen, Y. He, Y. Shao, X. Fu, G. Xiao, Appl. Catal. B 104 (2011) 30–36.
[30] G. Long, F. Fresno, S. Grosss, U.L. Stangar, Environ. Sci. Pollut. Res. Int. 21 (2014) 11189–11197.
[31] R. Rahimi, S. Zargari, M.M. Moghaddas, Adv. Mater. Res. 702 (2013) 172–175.
[32] M. Xie, X. Fu, L. Jing, P. Luan, Y. Feng, H. Fu, Adv. Energy Mater. 4 (2014) 130095.
[33] S. Ho-Kimur, S.J.A. Moniz, A.D. Handoko, J.W. Tang, J. Mater. Chem. A 2 (2014) 3948–3953.
[34] H. Li, H. Yu, X. Quan, S. Chen, H. Zhao, Adv. Funct. Mater. 25 (2015) 3074–3080.
[35] X. Zhu, F. Zhang, M. Wang, X. Gao, Y. Luo, J. Xue, Y. Zhang, J. Ding, S. Sun, C. Gao, Appl. Catal. A 15 (2015) 30194.
[36] M. Zalfani, B. Van Der Schueren, Z.Y. Hu, J. Rooke, R. Bourguiga, M. Wu, G. Van Tendeloo, Y. Li, B.L. Su, J. Mater. Chem. A 3 (2015) 21244–21256.
[37] M. Zalfani, B. van der Schueren, M. Mahdouani, R. Bourguiga, W.B. Yu, M. Wu, O. Deparis, Y. Li, B.L. Su, Appl. Catal. B (2016) 187–198.
[38] M. Wu, J. Liu, J. Jin, C. Wang, S.Z. Huang, Z. Deng, Y. Li, B.L. Su, Appl. Catal. B 150–151 (2014) 411–420.
[39] M. Wu, J. Jin, J. Liu, O. Deparis, B.L. Su, J. Mater. Chem. A 1 (2013) 15491–15500.
[40] M. Wu, A. Zheng, F. Deng, B.L. Su, Appl. Catal. B 138–139 (2013) 219–228.
[41] M. Wu, Y. Li, Z. Deng, B.L. Su, ChemSusChem 4 (2011) 1481–1488.
[42] S.D. Richardson, C.S. Wilson, K.A. Rusch, Ground Water 42 (2004) 678.
[43] D. Kornbrust, T. Barfknecht, Environ. Mutagen. 7 (1985) 101.
[44] D.B. McGregor, A.G. Brown, S. Howgate, D. McBride, C. Riach, W.J. Caspary, Environ. Mol. Mutagen. 199 (17) (2016) 196.
[45] Q. Wang, C.C. Chen, D. Zhao, W.H. Ma, J.C. Zhao, Langmuir 24 (2008) 7338.
[46] F. Chen, J.C. Zhao, H. Hidaka, Int. J. Photoenergy 5 (2003) 209.
[47] X.F. Hu, T. Mohamood, W.H. Ma, C.C. Chen, J.C. Zhao, J. Phys. Chem. B 110 (2006) 26012.
[48] S.K. Kansal, M. Singh, D. Sud, J. Hazard. Mater. 141 (2007) 581–590.
[49] K. Yu, S. Yang, H. He, C. Sun, C. Gu, Y. Ju, J. Phys. Chem. A 113 (2009) 10024–10032.
[50] M. Sun, D. Li, Y. Chen, W. Chen, W. Li, Y. He, X. Fu, J. Phys. Chem. C 113 (2009) 13825–13831.
[51] Z. He, C. Sun, S. Yang, Y. Ding, H. He, Z. Wang, J. Hazard. Mater. 162 (2009) 1477–1486.
[52] J. Luan, M. Li, K. Ma, Y. Li, Z. Zou, Chem. Eng. J. 167 (2011) 62–171.
[53] A. Mehrdad, B. Massoumi, R. Hashemzadeh, Chem. Eng. J. 168 (2011) 1073–1078.
[54] Y. Huang, H. Li, M.S. Balogun, W. Liu, Y. Tong, X. Lu, H. Ji, ACS Appl. Mater. Interfaces 6 (2014) 22920–22927.
[55] L. Chen, Q. Zhang, R. Huang, S.F. Yin, S.L. Luo, C.T. Au, Dalton Trans. 41 (2012) 9513–9518.
[56] C.J. Li, P. Zhang, R. Lv, J.W. Lu, T. Wang, S.P. Wang, H.F. Wang, J.L. Gong, Small 9 (2013) 3951.
[57] X. Xue, W. Ji, Z. Mao, H. Mao, Y. Wang, X. Wang, W. Ruan, B. Zhao, J.R. Lombardi, J. Phys. Chem. C 116 (2012) 8792–8797.
[58] C. Kim, K.S. Kim, H.Y. Kim, Y.S. Han, J. Mater. Chem. 18 (2008) 5809–5814.
[59] M. Shang, W. Wang, L. Zhou, S. Sun, W. Yin, J. Hazard. Mater. 172 (2009) 338.
[60] B. Cheng, W. Wang, L. Shi, J. Zhang, J. Ran, H. Yu, Int. J. Photoenergy (2012) 1.
[61] Z. Xiong, L.L. Zhang, J. Ma, X.S. Zhao, Chem. Commun. 46 (2010) 6011–6099.
[62] J. Su, L. Guo, N. Bao, C.A. Grimes, Nano Lett. 11 (2011) 1928–1933.
[63] Y. Fu, X. Sun, X. Wang, Mater. Chem. Phys. 131 (2011) 325.